

Article

Effects of Barrier Stiffness on Debris Flow Dynamic Impact—I: Laboratory Flume Test

Yu Huang ^{1,2,*} , Xiaoyan Jin ¹ and Junji Ji ¹

¹ Department of Geotechnical Engineering, College of Civil Engineering, Tongji University, Shanghai 200092, China; jinxiaoyan96@163.com (X.J.); jijunji1993@163.com (J.J.)

² Key Laboratory of Geotechnical and Underground Engineering of the Ministry of Education, Tongji University, Shanghai 200092, China

* Correspondence: yhuang@tongji.edu.cn; Tel.: +86-21-6598-2384; Fax: +86-21-6598-5210

Abstract: Debris flows often cause local damage to engineering structures by exerting destructive impact forces. The debris-flow–deformable-barrier interaction is a significant issue in engineering design. In this study, a large physical flume model test device was independently designed to repeatedly reproduce the flow and impact process of debris flow. Three physical flume tests were performed to investigate the effect of barrier stiffness on the debris flow impact. The flow kinematics of debris flow with three barrier stiffness values are essentially consistent with the process of impact–run-up–falling–pile-up. The development of a dead zone provided a cushion to diminish the impact of the follow-up debris flow on the barrier. The peak impact forces were attenuated as the barrier stiffness decreased. The slight deflections of a deformable barrier were sufficiently effective for peak load attenuation by up to 30%. It showed that the decrease of the barrier stiffness had a buffer effect on the debris flow impact and attenuated the peak impact force. And with the decrease of the barrier stiffness, when the barrier was impacted by the same soil types, the recoverable elastic strain will be larger, and the strain peak will be more obvious.

Keywords: deformable barrier; debris flow; flume tests; impact



Citation: Huang, Y.; Jin, X.; Ji, J.

Effects of Barrier Stiffness on Debris Flow Dynamic Impact—I: Laboratory Flume Test. *Water* **2022**, *14*, 177. <https://doi.org/10.3390/w14020177>

Academic Editor: Maria Mimikou

Received: 23 November 2021

Accepted: 5 January 2022

Published: 10 January 2022

Publisher's Note: MDPI stays neutral with regard to jurisdictional claims in published maps and institutional affiliations.



Copyright: © 2022 by the authors. Licensee MDPI, Basel, Switzerland. This article is an open access article distributed under the terms and conditions of the Creative Commons Attribution (CC BY) license (<https://creativecommons.org/licenses/by/4.0/>).

1. Introduction

Flow-like landslides are differentiated from landslides by the pervasive, fluid-like deformation of the mobilized material [1]; in addition, they typically contain high energy, can move with high velocity (>5 m/s), and travel relatively long distances [2]. It is difficult to classify those that present highly concentrated mixtures of water and solid material. Examples of flow-like landslides are rock avalanches, debris flow, sensitive clay flowslides and mud flows, and so on [3]. Moreover, such disasters often occur in mountainous terrain, and particularly in areas with steep terrain such as deep valleys and ravines. In China, mountainous and hilly areas account for approximately 65% of the land resource area. Hence, the geological conditions are complicated, and flow-like landslide disasters occur frequently and cause economic losses and casualties, often at a catastrophic scale [4]. For instance, the flow-like landslide that occurred in Maoxian, Sichuan, China, in June 2017, instantly destroyed the Xinmo village at the foot of the slope, demolishing 64 houses and resulting in 10 deaths. This landslide had a maximum speed of 74.6 m/s and traveled at a distance of 2.5 km [5]. In August 2010, a catastrophic debris flow occurred in Zhouqu, Gansu, China, and destroyed almost 5500 houses [6]. Protective structures are effective measures for mitigating debris flows. Prevention and control measures for flow-like landslides can be divided into active measures and passive ones (Huebl et al., 2005). Active measures, such as disaster assessment, early warning systems, land planning, etc., lack a consideration of disaster mechanisms and are insufficient to reduce risk. Passive measures are engineering structures which are made of concrete, such as barriers, deflecting/catching dams, nets, and baffle piles [7–20]. Among them, rigid walls, such as check dams, are

commonly used to resist the impact of granular flows [8,11,21]. However, these protective measures are commonly destroyed by geo-flows and cause even more hazardous disasters owing to the large dynamic impact forces, which is the main damaging factor based on the statistical analysis of the failure types attributed to debris flow [21]. Hence, it is very important to investigate the dynamic impact of flow–structure interactions to design effective hazard mitigation structures.

Several physical modeling and numerical approaches have been proposed to evaluate the impact forces of geo-flows with satisfactory accuracy. Conducting laboratory experiments is an effective method for elucidating the dynamic impact characteristics of granular-flow–structure interactions because this method has high-repeatability and low-cost, in contrast to field-scale experiments. Nevertheless, the scaling problem is an unavoidable key consideration [22,23] when modelling debris flow in the flume test. Moreover, numerical simulations, such as the Moving Particles Semi-implicit Method [24], the Element-Free Galerkin Method [25], and the Finite Point Method [26], have been commonly implemented to investigate the impact dynamics of debris flow and assist in industrial design, owing to their advantage of wide applicability. Among them, the Smoothed Particle Hydrodynamics method (SPH) is robust and reliable for debris flows simulation [21,27–31]. For the reservoir considered in this study, the dynamics of debris flow impact on a deformable barrier were investigated through laboratory flume tests and numerical simulations. The authors focused on the analysis of the dynamics of debris flow impact on a deformable barrier based on laboratory experiments. The analysis of the impact dynamics based on the SPH method is presented in an accompanying paper [32].

Many laboratory experiments have been conducted to investigate the impact effect of debris flow on rigid barriers, baffles, and bent structures. Moriguchi et al. [1] investigated the effect of debris flow impact on a rigid baffle by conducting a flume test, and obtained the overall stress time history curve of the rigid baffle. Scheidl et al. [33] measured the time-history curve of the debris flow impact force exerted on rigid baffles by conducting a chute test, and investigated the relationship between the peak velocity and impact force. Many studies have extensively investigated the calculation of the soil flow impact force through laboratory experiments. Currently, the most critical step in barrier design is the estimation of the impact force, which is mostly based on simplified empirical models that can be categorized into two main types, namely, hydrostatic models and hydrodynamic models, according to fluid mechanics theory [34–36]. However, the empirical factors of these models have always been controversial and vary within a wide range. Moreover, these empirical models cannot reflect the complex interaction between actual granular flows and structures. For example, according to the study of Kwan et al. [37], the value of the dynamic empirical factors ranges from 0.6 to 2.0 for flexible barriers and from 2.5 to 5.0 for rigid barriers. Most existing studies have focused on the role of the properties of the granular materials in the impact characteristics for modeling structures considered as rigid bodies, whereas the influence of the deformable barrier stiffness on the impact characteristics has attracted little attention. The stiffness of structures plays an important part in dynamic impact. Based on elastoplastic theory, He et al. [38] proposed the theoretical calculation of the impact force of several common types of debris flow prevention structures in combination with tests, and found that the impact force of debris flows decreases with the retaining structure stiffness, which is similar to the simulated results obtained by Ashwood and Hungr [39]. In general, the effects of barrier stiffness on the impact force and structural deformation response still need to be further explored, and there is still a need for effective experimental means to capture the debris flow impact kinematics.

In this study, a large physical flume model testing device was independently designed to repeatedly reproduce the flow and impact process of debris flow. Three flume tests were conducted to investigate the effects of deformable barriers with different stiffness on the impact forces of debris flows. First, the flume tests and measurement devices are introduced. As is known, debris flows are multi-phase materials with complicated impact mechanisms. Sand can be used to simulate a simple case of debris flow so as to elucidate the fundamental

mechanisms of debris flow impact on deformable barriers. In this study, flume tests were carried out to investigate the effects of barrier stiffness on the flow kinematics and impact forces, and a flume model is proposed to analyze the dynamics of debris flow impact on deformable barriers. The proposed model can be used as a reference by similar studies.

2. Laboratory Flume Test

2.1. Flume Modelling

To investigate the impact characteristics, the complex debris-flow–deformable-barrier interaction was analyzed through tests on a prototype of the proposed flume model with a scale of 1:25. Figure 1 shows a photograph of the side view of the flume model. The physical model was made of steel with dimensions $4000 \times 400 \times 1500$ mm (length \times width \times height), and mainly comprised three parts as shown in Figure 1.

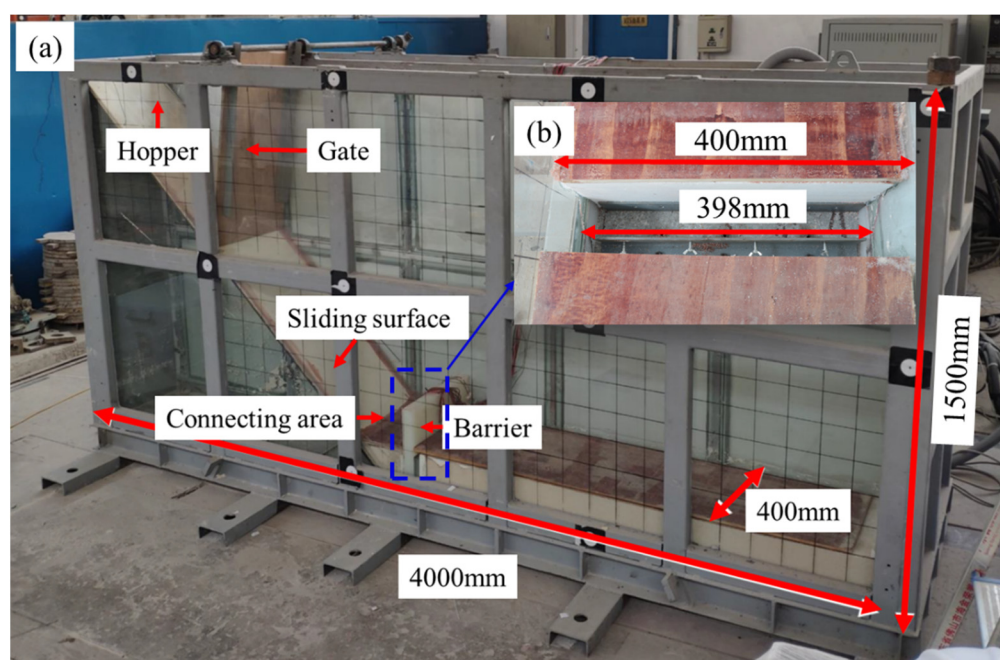


Figure 1. (a) Photograph of physical flume modelling instrumentation; (b) fixing bolts at the bottom of the barrier.

A hopper with stored sliding sand was used, and its release was controlled by an automatic gate, which was opened sufficiently fast to avoid affecting the initial flow characteristics of the sliding sand.

The sliding surface was made of wooden boards whose inclination angle was fixed at 45° , which effectively reduced the friction coefficient between the sliding sand and the sliding bed to assist in obtaining results with stronger impact dynamics, and the connection area between the acceleration plane and the run-out plane was made with silicone glue to ensure a smooth transition.

A barrier located at the bottom of the model was used to investigate the model's dynamic response under the impact of sand flow and under different stiffness conditions. The barrier (398 mm width) bolted to the run-out plane had a small gap between the two sides of the boundary (400 mm width) to ensure that the structure can freely deform under the action of debris flow to minimize the boundary effect (Figure 1b).

Since this test aims to explore the general impact characteristics of debris flow on barrier, and there is no definite landslide example as the prototype, the size similarity ratio is determined to be 25. Because that the model test was carried out in the conventional gravity environment, the acceleration similarity ratio is 1. In the experiment, materials with density similar to that of the landslide site were used, so the density similarity ratio was 1.

At the same time, in order to ensure that the landslide movement driven by gravity meets the dynamic similarity, the Froude similarity [40] was used in this paper and set as 1.

2.2. Parameters of Barrier Design

The barrier design mainly considered the height, thickness, and elastic modulus. The barrier height was set to 300 mm to consider the structural response characteristics under non-overflow conditions. Moreover, the barrier was bolted to the run-out plane and buried at sufficient depth (180 mm) to resist the sand flow and ensure that the barrier could not be swept away. According to “Design and Construction of landslide prevention engineering” (DZ/T 0219-2006), when rubble concrete or plain concrete is used to construct a gravity retaining wall, the top width of rubble concrete or regular concrete barrier should not be less than 0.6 m. To obtain the frontal impact force of the sliding body, a retaining wall type with a rectangular section and thickness of 45 mm was adopted in this study. The barrier dimensions were $398 \times 45 \times 480$ mm (length \times width \times height). The characteristics of barrier are listed in Table 1. In the experiment, polypropylene (PP) was selected to simulate a barrier with an elastic modulus of 1.0 GPa. Moreover, low-density polyethylene (LDPE) and high-density polyethylene (HDPE) plates were used to simulate barriers with different stiffness, and their elastic modulus was 0.6 GPa and 0.8 GPa, respectively. The HDPE material has higher rigidity and toughness, as well as higher strength and hardness compared with LDPE. The PP material has high crystallinity, complete structure, and higher mechanical properties; the tensile strength, hardness, and elasticity are higher compared with HDPE.

Table 1. Characteristics of barrier.

Barrier Materials	Barrier Height (H: mm)	Young’s Modulus (E: GPa)	Poisson’s Ratio (ν : \)	Test ID
Low-density polyethylene (LDPE)	300	0.6	0.30	S_6
High-density polyethylene (HDPE)	300	0.8	0.30	S_8
Polypropylene (PP)	300	1.0	0.30	S_10

2.3. Instrumentation

To measure the loading and deformation, six sensors for measuring the impact force and six groups of strain gates, named L1, L2, L3, L4, L5, and L6, and S1, S2, S3, S4 S5, and S6 from bottom to top, respectively, were installed along the upstream wall of the barrier, as shown in Figure 2a. The high-speed camera was i-Speed 716 (Figure 2b), with functions including fast multiple sampling of high-speed targets in very short time, real-time target capture, fast image recording, instant playback, and intuitive and clear images. The high-speed camera was i-Speed 716 (Figure 2b), with functions including fast multiple sampling of high-speed targets in very short time, real-time target capture, fast image recording, instant playback, and intuitive and clear images. The following described the parameters of the high-speed camera:

- High resolution pixel sensor: 2048×1536
- 7540 fps @ 1080 p
- Ultra-high speed 16 GP/sec data bandwidth
- Maximum frame rate: 500,000 fps
- Frame synchronization: 24 Hz–500 kHz

The full resolution capability of the camera used in this test is 2048×1536 pixels and its sampling frequency is up to 1000 frames per second. The high-speed camera has its own video capture system, i-Speed Software Suite 2.0 (see Figure 2b), which can control high-speed camera through computer. The two sides of the model were made of transparent

toughened glass to observe the flow process of the sand material, and a high-speed camera was set on the side to capture the flow kinematics of the debris flow.

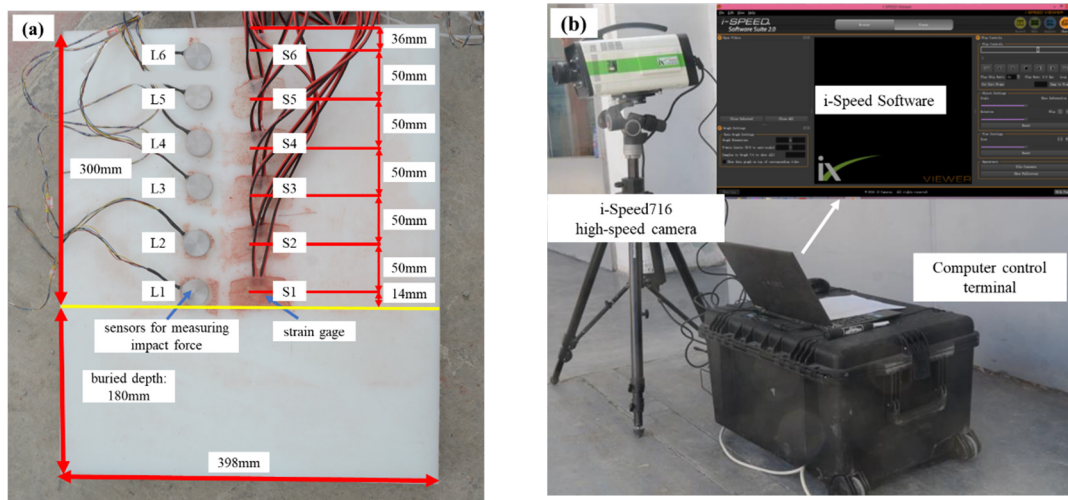


Figure 2. (a) Impact loading sensors, strain gates, and distribution; (b) high-speed recording system.

2.4. Test Materials and Scheme

Flume tests were conducted on dry, fine sand to investigate the dynamics of debris flow impact on a deformable barrier. Debris flows are multi-phase materials with complicated impact mechanisms, and sand can be used to simulate a simple case of debris flow so as to elucidate the fundamental mechanisms of debris flow impact on deformable barriers. The experimental sand materials can be categorized into three sizes: maximum grain size ($d \approx 1 \text{ mm}$), medium grain size ($d \approx 0.5 \text{ mm}$), and minimum grain size ($d \approx 0.25 \text{ mm}$). The tested sand had fine grain size, that is, $D_{10} = 0.3 \text{ mm}$ and $D_{60} = 0.7 \text{ mm}$, and a coefficient of uniformity of 2.3. The grain size curve of the material was shown in Figure 3. The maximum, minimum, and bulk dry density obtained through density tests was 1.53 g/cm^3 , 1.32 g/cm^3 , and 1.40 g/cm^3 , respectively. Inclining tests and direct shear tests revealed that the internal friction angle of sand was 34° . The cohesion of sand was $c = 0 \text{ Pa}$. Additionally, it was ensured that the hopper could be filled with sand until the same horizontal position to obtain the same initial conditions each time. Three test cases were considered and analyzed to obtain fundamental insights regarding the impact dynamics of debris flow under different barrier stiffness. The key parameters of dry sand are summarized in Table 2.

Table 2. Key parameters of dry sand.

Material Property		Parameters
Maximum grain size	$d \text{ (mm)}$	1.00
Medium grain size	$d \text{ (mm)}$	0.50
Minimum grain size	$d \text{ (mm)}$	0.25
Coefficient of uniformity		2.3
Maximum dry density	$\gamma_{\text{max}} \text{ (g/cm}^3\text{)}$	1.53
Minimum dry density	$\gamma_{\text{min}} \text{ (g/cm}^3\text{)}$	1.32
Bulk density	$\gamma \text{ (g/cm}^3\text{)}$	1.40
Cohesion	$c \text{ (kPa)}$	0.0
Angle of internal friction	$\varphi \text{ (}^\circ\text{)}$	34

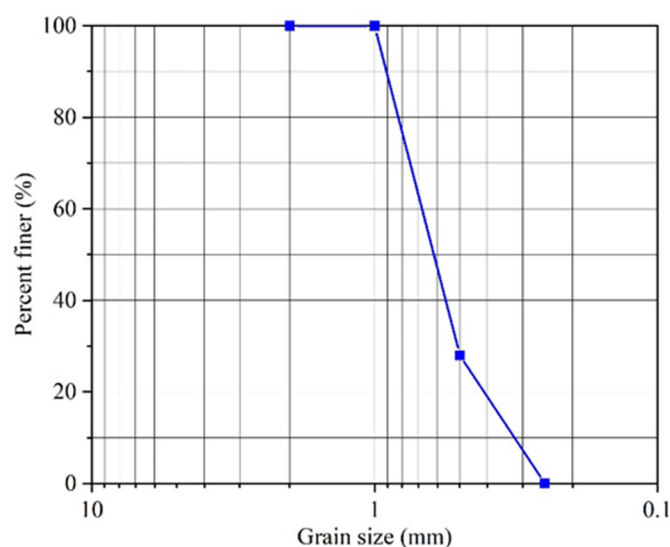


Figure 3. The grain size curve of the material.

3. Debris Flow Velocity Measurements and Impact Signal Processing

Particle Image Velocimetry (PIV) technology, which was first introduced into geotechnical testing by White et al. [41,42], is a velocity measurement technique that can help in recognizing the individual tracer debris particles and analyzing their flow paths and velocity during the evolution of debris flow through the analysis of images with high resolution and picture quality. The debris flow analysis used in PIVlab [43,44] typically measures the flow velocity by identifying the distance travelled from the features of two images (X and Y) at different time periods (t_0 and $t_0 + \Delta t$). The images provided by PIVlab contain all positions $P(x,y)$, speed, and displacement of debris particles. Particularly, to increase the texture characteristics of debris particles and distinguish different test windows, the sand was partially dyed red before the test, and mixed with another part of the test sand after drying.

Only the images pertaining to the analysis of flow velocity and the recognition of the position of debris particles were processed by PIVlab. The dynamic impact forces and structural response strain were obtained using the previously mentioned sensors for measuring the impact force and strain gauge, respectively. However, the impact signal of debris flow is a typical non-stationary signal, and all signals collected by the sensors include noise. This study used the wavelet de-noising method to deal with the collected impact signals. After performing several analyses on the test results, the Daubechies (dbN) wavelet [45] was selected to conduct 4-layer one-dimensional multi-scale denoising on the collected signals to obtain data representing the actual signal without the noise.

4. Interpretation of Test Results

4.1. Observed Debris Flow Impact Kinematics

In all results, time t began as the granular flow hit the barrier. Figure 4 shows the velocity field of the flows through the PIV [41,42] for test ID: S_6 at several instances. At time $t = 0.0$ s, a wedge-like flow approached the barrier with a maximum frontal velocity of approximately 3.1 m/s. At 0.11 s, the flow front impacted the barrier and the maximum velocity decreased by approximately 20% to 2.7 m/s. A dead zone gradually formed near the wall, and the loading of the barrier gradually reached the peak. Then, the subsequent flow overtopped the dead-zone, which exerted the effect of a cushion layer, and then began to run up along the surface of the barrier and fell back after reaching the top. The development of the dead zone provided a cushion that diminished the impact of the follow-up debris flow on the barrier. At $t = 0.50$ s, the maximum velocity was 1.6 m/s, the size of the dead zone increased and piled up behind the barrier and progressively reached static equilibrium. At $t = 1.16$ s, the frontal velocity of the debris flow dropped

to 0.0 m/s and reached the state of static pile up. The debris flow kinematics under the barrier stiffness of 0.8 GPa and 1.0 GPa (test ID: S_8 and test ID: S_10, respectively) are essentially consistent with those obtained in test ID: S_6, that is, they are consistent with the impact–run-up–falling–pile-up process.

4.2. Effects of Barrier Stiffness on Peak Impact

Figure 5a,b shows the evolution of the total impact forces (summed through L1, L2, L3, L4, L5, and L6) and strain (S1, S2, S3, S4, S5, and S6) of the barrier when the peak impact occurred under three different stiffness values, respectively. Figure 5a showed that the impact forces of each barrier obviously peaked at approximately $t = 0.1$ s and then decreased to static states that generated static earth pressure at approximately $t = 0.5$ s, which corresponds to the observation in Section 4.1. The comparison of the peak pressure between the impact time histories of different barriers reveals the existence of attenuation with the decrease of the barrier stiffness. As shown in Figure 5, the respective peak impact force strongly evolved with the barrier stiffness. The peak impact forces obtained for the barrier were 11.7 kPa, 17.3 kPa, and 20.4 kPa with $E = 0.6$ GPa, $E = 0.8$ GPa, and $E = 1.0$ GPa, respectively. Lower stiffness attenuated the peak load by approximately 30% for fine sand flow. Intuitively, from the hydrodynamic equation $F = \alpha \rho v^2 h L$ [46] (where α represents the dynamic impact coefficient; ρ represents the debris flow density [kg/m^3]; v represents the frontal velocity before impact; and h and L represent the debris flow depth and barrier width [m], respectively), the sand flow has a thick flow depth h with large velocity v (Figure 4), which induces a large frontal impact force. The peak impact load was three times larger than the static load, which left sufficient space for deflection by the barrier. In turn, the deformation of the barrier played a buffer role in the flow–barrier interaction.

At $t = 0.11$ s, the barrier strained when the peak pressure occurred, owing to the frontal flow, as shown in Figure 5b. The maximum deformation occurred near the base of the maximum impact force. Almost no deformation was observed with a barrier height less than twice the flow depth before impact. However, peak deflection was clearly observed for the minimum barrier stiffness and became slighter as the structural stiffness increased (Figure 5b). Upon impact, the peak impact force carried larger kinetic energy, which increased the deflection of the barrier until the static state. Moreover, an obvious peak value of $188 \mu\epsilon$ was observed under the barrier stiffness of 0.6 GPa, and became less apparent as the barrier stiffness increased. As sand was gradually deposited behind the flexible barrier during impact, the elastic rebound of the barrier mobilized the shear energy consumption of the flow layer and dead zone, and caused peak impact load attenuation. Song et al. [46] considered that the deformable barrier can substantially attenuate the impact loads only when the deflection approaches the flow depth. Nevertheless, in this study, a strain increase of only $90 \mu\epsilon$ (Figure 5c) could attenuate up to 30% of the peak impact force with a barrier stiffness of 1.0 GPa (peak impact force 20.4 Kpa, test S_10) to 0.6 GPa (peak impact force 11.7 Kpa, test S_6). This implies that the slight deflections of the deformable barrier were sufficient for peak load attenuation, which is consistent with the study of Ng et al. [47].

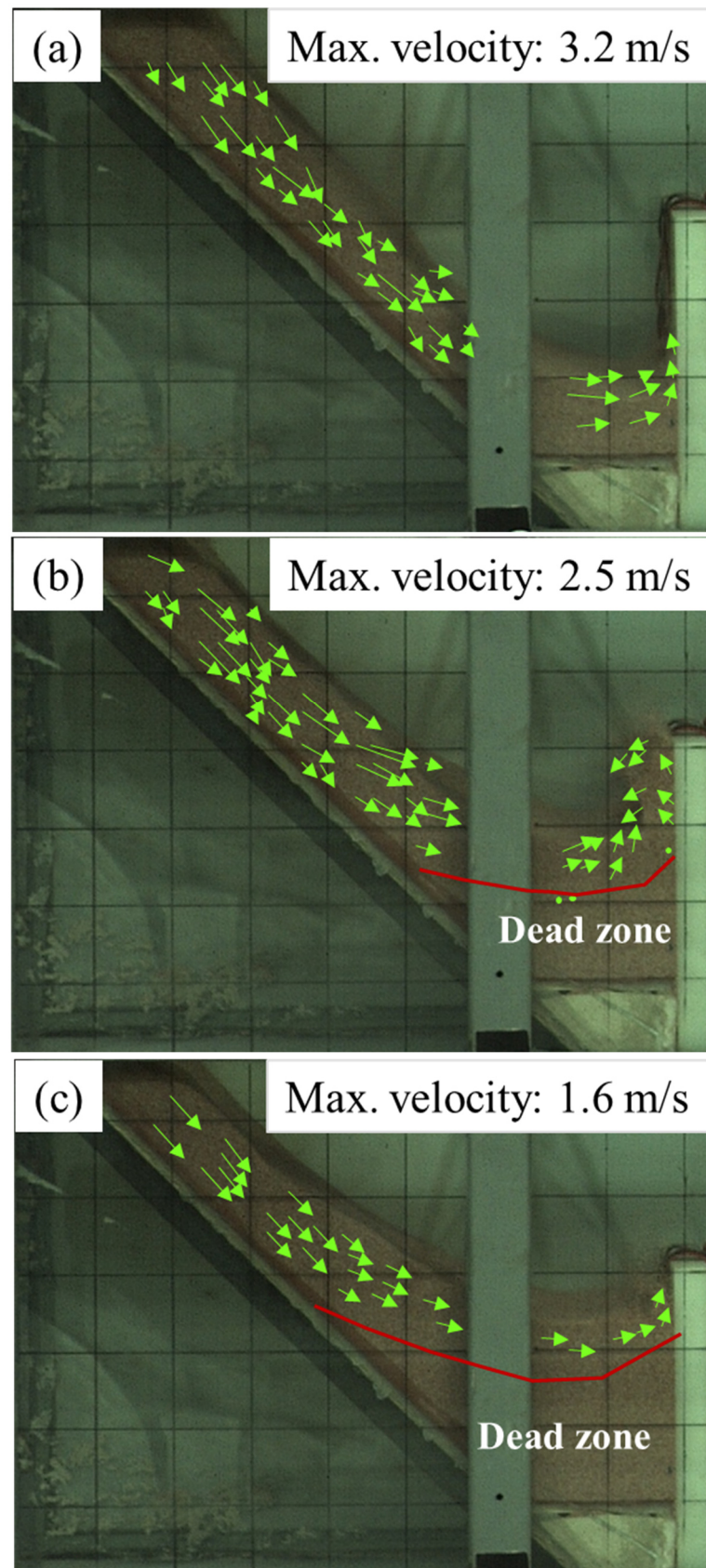


Figure 4. Velocity field of flows at different times obtained from PIV (test ID: S_10): (a) $t = 0.00$ s; and (b) $t = 0.11$ s; (c) $t = 0.50$ s.

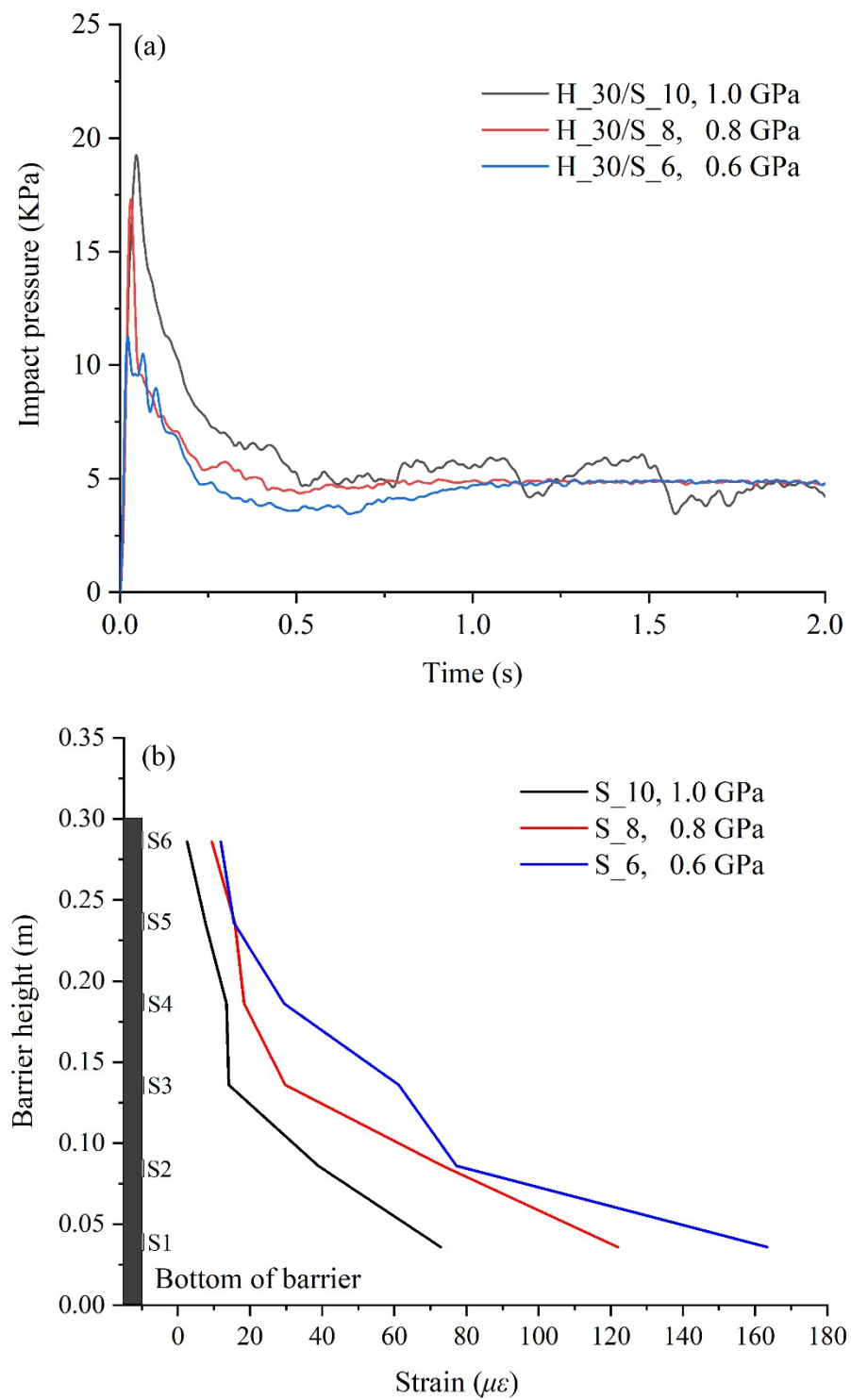


Figure 5. Cont.

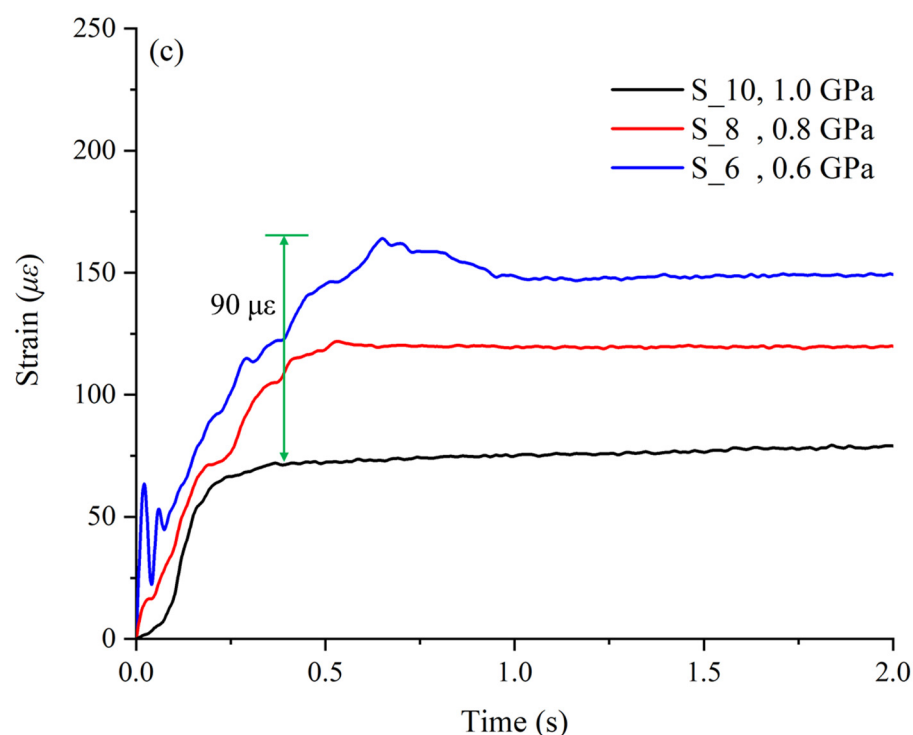


Figure 5. (a) Impact force time history curve with different barrier stiffness; (b) strain of barrier when peak impact force occurred; and (c) total strain time history curve of different stiffness of barrier.

5. Discussion

This paper only addresses some of the fundamental aspects of the effects of barrier stiffness on debris flow dynamic impact. Due to the complex unsteady flow characteristics of debris flow, there is still a need for a lot of field test data and the numerical simulation method of high performance to further exploration.

In this study, only dry, fine sand was used. However, flow-like landslides in the natural state present mixtures of water, air and solid grains with different size [3], which may play a crucial role in flow–structure interaction process [48]. Jiang et al. [49] used three kinds of natural soil materials to study the influence of internal friction angle and particle size on impact characteristics, and the results showed that particle characteristics have a great influence on impact force. Song et al. [50] studied the impact characteristics of debris flow entrained pebbles on rigid structures in the centrifuge model, and found that with the increase of pebble particle size, the impact signals pulse. The increase of coarse particles leads to the enhancement of debris flow impact damage. Moreover, the viscous effect of interstitial fluid in real debris flow will affect the flow impact characteristics [17,51–53] revealed that different rheology behavior of viscous flow and frictional flow would exhibit totally different impact mechanism even with identical Froude characteristics. Song et al. [17] investigated the influence of solid fraction on debris flow impact mechanism and found that the flow mobility will be enhanced by interstitial fluid. Therefore, the impact characteristics of different particle sizes and different flow behavior on different stiffness structures and the dynamic response characteristics of structures themselves need further experimental and numerical research.

6. Conclusions

The investigation of the dynamic impact behavior of flow–structure interactions is very important for the design of hazard mitigation structures. This study quantitatively analyzed the effects of barrier stiffness on impact dynamics based on self-designed flume test equipment. The main conclusions drawn from this study are as follows:

- (1) The flow kinematics of debris flow observed under three barrier stiffness values are essentially consistent with the impact–run-up–falling–pile-up process. The development of a dead zone provided a cushion that diminished the impact of the follow-up debris flow on the barrier.
- (2) The respective peak impact force evolved strongly with the barrier stiffness. The peak impact forces attenuated with the decrease of the barrier stiffness, which is attributed to the barrier deformation playing a buffer role in flow–structure interaction with lower stiffness.
- (3) Notably, even the slight deflections of the deformable barrier were sufficient for peak load attenuation by up to 30%. As the barrier stiffness decreased, the recoverable elastic strain became larger and the strain peak was more obvious when the debris flow made impact.

Author Contributions: Conceptualization, Y.H.; methodology, X.J. and J.J.; validation, X.J. and J.J.; formal analysis, X.J. and J.J.; investigation, X.J. and J.J.; data curation, X.J. and J.J.; writing—original draft preparation, X.J.; writing—review and editing, X.J.; visualization, X.J.; supervision, Y.H.; project administration, Y.H.; funding acquisition, Y.H. All authors have read and agreed to the published version of the manuscript.

Funding: This work was supported by the National Natural Science Foundation of China (grant No. 41831291).

Institutional Review Board Statement: Not applicable.

Informed Consent Statement: Not applicable.

Acknowledgments: The authors thank the editor and the reviewers for their help to improve the quality of our manuscript.

Conflicts of Interest: The authors declare no conflict of interest.

References

1. Moriguchi, S.; Borja, R.I.; Yashima, A.; Sawada, K. Estimating the impact force generated by granular flow on a rigid obstruction. *Acta Geotech.* **2009**, *4*, 57–71. [[CrossRef](#)]
2. Huang, Y.; Zhang, B.; Zhu, C. Computational assessment of baffle performance against rapid granular flows. *Landslides* **2021**, *18*, 485–501. [[CrossRef](#)]
3. Hungr, O.; Leroueil, S.; Picarelli, L. The Varnes classification of landslide types, an update. *Landslides* **2014**, *11*, 167–194. [[CrossRef](#)]
4. Dowling, C.A.; Santi, P.M. Debris flows and their toll on human life: A global analysis of debris-flow fatalities from 1950 to 2011. *Nat. Hazards* **2014**, *71*, 203–227. [[CrossRef](#)]
5. Xu, Q.; Li, W.; Dong, X.; Xiao, X.; Fan, X.; Pei, X. The Xinmocun landslide on 24 June 2017 in Maoxian, Sichuan: Characteristics and failure mechanism. *Chin. J. Rock Mech. Eng.* **2017**, *36*, 2612–2628.
6. Tang, C.; van Asch, T.W.J.; Chang, M.; Chen, G.Q.; Zhao, X.H.; Huang, X.C. Catastrophic debris flows on 13 August 2010 in the Qingping area, southwestern China: The combined effects of a strong earthquake and subsequent rainstorms. *Geomorphology* **2012**, *139–140*, 559–576. [[CrossRef](#)]
7. Abdelrazek, A.M.; Kimura, I.; Shimizu, Y. Simulation of three-dimensional rapid free-surface granular flow past different types of obstructions using the SPH method. *J. Glaciol.* **2016**, *62*, 335–347. [[CrossRef](#)]
8. Armanini, A.; Rossi, G.; Larcher, M. Dynamic impact of a water and sediments surge against a rigid wall. *J. Hydraul. Res.* **2020**, *58*, 314–325. [[CrossRef](#)]
9. Bi, Y.-Z.; He, S.-M.; Li, X.-P.; Wu, Y.; Xu, Q.; Ouyang, C.-J.; Su, L.-J.; Wang, H. Geo-engineered buffer capacity of two-layered absorbing system under the impact of rock avalanches based on Discrete Element Method. *J. Mt. Sci.* **2016**, *13*, 917–929. [[CrossRef](#)]
10. Chen, H.-X.; Li, J.; Feng, S.-J.; Gao, H.-Y.; Zhang, D.-M. Simulation of interactions between debris flow and check dams on three-dimensional terrain. *Eng. Geol.* **2019**, *251*, 48–62. [[CrossRef](#)]
11. Jiang, Y.-J.; Fan, X.-Y.; Li, T.-H.; Xiao, S.-Y. Influence of particle-size segregation on the impact of dry granular flow. *Powder Technol.* **2018**, *340*, 39–51. [[CrossRef](#)]
12. Naaim, M.; Faug, T.; Naaim, F.; Eckert, N. Return period calculation and passive structure design at the Tacconnaz avalanche path, France. *Ann. Glaciol.* **2010**, *51*, 89–97. [[CrossRef](#)]
13. Ng, C.W.W.; Choi, C.E.; Liu, L.H.D.; Wang, Y.; Song, D.; Yang, N. Influence of particle size on the mechanism of dry granular run-up on a rigid barrier. *Geotech. Lett.* **2017**, *7*, 79–89. [[CrossRef](#)]
14. Remaitre, A.; van Asch, T.W.J.; Malet, J.P.; Maquaire, O. Influence of check dams on debris-flow run-out intensity. *Nat. Hazards Earth Syst. Sci.* **2008**, *8*, 1403–1416. [[CrossRef](#)]

15. Shen, W.; Wang, D.; Qu, H.; Li, T. The effect of check dams on the dynamic and bed entrainment processes of debris flows. *Landslides* **2019**, *16*, 2201–2217. [[CrossRef](#)]
16. Shen, W.; Zhao, T.; Zhao, J.; Dai, F.; Zhou, G.G.D. Quantifying the impact of dry debris flow against a rigid barrier by DEM analyses. *Eng. Geol.* **2018**, *241*, 86–96. [[CrossRef](#)]
17. Song, D.; Ng, C.W.W.; Choi, C.E.; Zhou, G.G.D.; Kwan, J.S.H.; Koo, R.C.H. Influence of debris flow solid fraction on rigid barrier impact. *Can. Geotech. J.* **2017**, *54*, 1421–1434. [[CrossRef](#)]
18. Teufelsbauer, H.; Wang, Y.; Chiou, M.-C.; Wu, W. Flow–obstacle interaction in rapid granular avalanches: DEM simulation and comparison with experiment. *Granul. Matter* **2009**, *11*, 209–220. [[CrossRef](#)]
19. Teufelsbauer, H.; Wang, Y.; Pudasaini, S.P.; Borja, R.I.; Wu, W. DEM simulation of impact force exerted by granular flow on rigid structures. *Acta Geotech.* **2011**, *6*, 119–133. [[CrossRef](#)]
20. Zhou, G.G.D.; Song, D.; Choi, C.E.; Pasuto, A.; Sun, Q.C.; Dai, D.F. Surge impact behavior of granular flows: Effects of water content. *Landslides* **2018**, *15*, 695–709. [[CrossRef](#)]
21. Dai, Z.; Huang, Y.; Cheng, H.; Xu, Q. SPH model for fluid–structure interaction and its application to debris flow impact estimation. *Landslides* **2017**, *14*, 917–928. [[CrossRef](#)]
22. Khan-Mozahedy, A.B.M.; Muñoz-Perez, J.J.; Neves, M.G.; Sancho, F.; Cavique, R. Mechanics of the scouring and sinking of submerged structures in a mobile bed: A physical model study. *Coast. Eng.* **2016**, *110*, 50–63. [[CrossRef](#)]
23. Chen, J.; Chen, X.; Zhao, W.; You, Y. Debris Flow Drainage Channel with Energy Dissipation Structures: Experimental Study and Engineering Application. *J. Hydraul. Eng.* **2018**, *144*, 06018012. [[CrossRef](#)]
24. Nohara, S.; Suenaga, H.; Nakamura, K. Large deformation simulations of geomaterials using moving particle semi-implicit method. *J. Rock Mech. Geotech. Eng.* **2018**, *10*, 1122–1132. [[CrossRef](#)]
25. Wang, C.; Deng, A.; Taheri, A.; Ge, L. A Mesh-Free Approach for Multiscale Modeling in Continuum–Granular Systems. *Int. J. Comput. Methods* **2020**, *17*, 2050006. [[CrossRef](#)]
26. Qin, X.; Hu, G.; Peng, G. Finite point method of nonlinear convection diffusion equation. *Filomat* **2020**, *34*, 1517–1533. [[CrossRef](#)]
27. Huang, Y.; Zhang, W.; Xu, Q.; Xie, P.; Hao, L. Run-out analysis of flow-like landslides triggered by the Ms 8.0 2008 Wenchuan earthquake using smoothed particle hydrodynamics. *Landslides* **2012**, *9*, 275–283. [[CrossRef](#)]
28. Li, S.; Peng, C.; Wu, W.; Wang, S.; Chen, X.; Chen, J.; Zhou, G.G.; Chitneedi, B.K. Role of baffle shape on debris flow impact in step-pool channel: An SPH study. *Landslides* **2020**, *17*, 2099–2111. [[CrossRef](#)]
29. Monaghan, J.J.; Kos, A.; Issa, N. Fluid Motion Generated by Impact. *J. Waterw. Port Coast. Ocean Eng.* **2003**, *129*, 250–259. [[CrossRef](#)]
30. Pastor, M.; Yague, A.; Stickler, M.M.; Manzanal, D.; Mira, P. A two-phase SPH model for debris flow propagation. *Int. J. Numer. Anal. Methods Géoméch.* **2018**, *42*, 418–448. [[CrossRef](#)]
31. Wang, W.; Chen, G.; Han, Z.; Zhou, S.; Zhang, H.; Jing, P. 3D numerical simulation of debris-flow motion using SPH method incorporating non-Newtonian fluid behavior. *Nat. Hazards* **2016**, *81*, 1981–1998. [[CrossRef](#)]
32. Huang, Y.; Jin, X.Y.; Ji, J.J. Effects of barrier stiffness on debris flow dynamic impact—II: Numerical simulation. *Water*, in press.
33. Scheidl, C.; Chiari, M.; Kaitna, R.; Müllegger, M.; Krawtschuk, A.; Zimmermann, T.; Proske, D. Analysing Debris-Flow Impact Models, Based on a Small Scale Modelling Approach. *Surv. Geophys.* **2013**, *34*, 121–140. [[CrossRef](#)]
34. Laigle, D.; Lachamp, P.; Naaim, M. SPH-based numerical investigation of mudflow and other complex fluid flow interactions with structures. *Comput. Geosci.* **2007**, *11*, 297–306. [[CrossRef](#)]
35. Cui, P.; Zeng, C.; Lei, Y. Experimental analysis on the impact force of viscous debris flow. *Earth Surf. Process. Landf.* **2015**, *40*, 1644–1655. [[CrossRef](#)]
36. Bugnion, L.; McArdell, B.W.; Bartelt, P.; Wendeler, C. Measurements of hillslope debris flow impact pressure on obstacles. *Landslides* **2012**, *9*, 179–187. [[CrossRef](#)]
37. Kwan, J.S.H.; Chan, S.L.; Cheuk, J.C.Y.; Koo, R.C.H. A case study on an open hillside landslide impacting on a flexible rockfall barrier at Jordan Valley, Hong Kong. *Landslides* **2014**, *11*, 1037–1050. [[CrossRef](#)]
38. He, S.; Wu, Y.; Shen, J. Simplified calculation of impact force of massive stone in debris flow. *J. Nat. Disasters* **2009**, *18*, 51–56.
39. Ashwood, W.; Hungr, O. Estimating total resisting force in flexible barrier impacted by a granular avalanche using physical and numerical modeling. *Can. Geotech. J.* **2016**, *53*, 1700–1717. [[CrossRef](#)]
40. Rickenmann, D. Empirical Relationships for Debris Flows. *Nat. Hazards* **1999**, *19*, 47–77. [[CrossRef](#)]
41. Adrian, R.J. Particle-imaging techniques for experimental fluid-mechanics. *Annu. Rev. Fluid Mech.* **1991**, *23*, 261–304. [[CrossRef](#)]
42. White, D.J.; Take, W.A.; Bolton, M.D. Soil deformation measurement using particle image velocimetry (PIV) and photogrammetry. *Geotechnique* **2003**, *53*, 619–631. [[CrossRef](#)]
43. Keane, R.D.; Adrian, R.J. Theory of cross-correlation analysis of PIV images. *Appl. Sci. Res.* **1992**, *49*, 191–215. [[CrossRef](#)]
44. Utami, T.; Blackwelder, R.F.; Ueno, T. A cross-correlation technique for velocity field extraction from particulate visualization. *Exp. Fluids* **1991**, *10*, 213–223. [[CrossRef](#)]
45. Abdolmaleki, M.; Tabaei, M.; Fathianpour, N.; Gorte, B.G.H. Selecting optimum base wavelet for extracting spectral alteration features associated with porphyry copper mineralization using hyperspectral images. *Int. J. Appl. Earth Obs. Geoinf.* **2017**, *58*, 134–144. [[CrossRef](#)]
46. Song, D.; Zhou, G.G.D.; Xu, M.; Choi, C.E.; Li, S.; Zheng, Y. Quantitative analysis of debris-flow flexible barrier capacity from momentum and energy perspectives. *Eng. Geol.* **2019**, *251*, 81–92. [[CrossRef](#)]

47. Ng, C.W.W.; Wang, C.; Choi, C.E.; De Silva, W.A.R.K.; Poudyal, S. Effects of barrier deformability on load reduction and energy dissipation of granular flow impact. *Comput. Geotech.* **2020**, *121*, 103445. [[CrossRef](#)]
48. Zhang, B.; Huang, Y. Unsteady overflow behavior of polydisperse granular flows against closed type barrier. *Eng. Geol.* **2021**, *280*, 105959. [[CrossRef](#)]
49. Jiang, Y.-J.; Zhao, Y.; Towhata, I.; Liu, D.-X. Influence of particle characteristics on impact event of dry granular flow. *Powder Technol.* **2015**, *270*, 53–67. [[CrossRef](#)]
50. Song, D.; Choi, C.E.; Zhou, G.G.D.; Kwan, J.S.H.; Sze, H.Y. Impulse load characteristics of bouldery debris flow impact. *Géotech. Lett.* **2018**, *8*, 111–117. [[CrossRef](#)]
51. Choi, C.E.; Au-Yeung, S.C.H.; Ng, C.W.W.; Song, D. Flume investigation of landslide granular debris and water runup mechanisms. *Géotech. Lett.* **2015**, *5*, 28–32. [[CrossRef](#)]
52. Song, D.; Choi, C.E.; Ng, C.W.W.; Zhou, G.G.D. Geophysical flows impacting a flexible barrier: Effects of solid-fluid interaction. *Landslides* **2018**, *15*, 99–110. [[CrossRef](#)]
53. Zhou, G.G.D.; Cui, K.F.E.; Jing, L.; Zhao, T.; Song, D.; Huang, Y. Particle Size Segregation in Granular Mass Flows With Different Ambient Fluids. *J. Geophys. Res. Solid Earth* **2020**, *125*, e2020JB019536. [[CrossRef](#)]